Cavity alignment using fringe scanning

LIGO SURF Final Report

Laura Paulina Šinkūnaitė
University of Glasgow, United Kingdom

Mentors
Dr. Michael Landry
Dr. Keita Kawabe

22^{nd} of December 2015

Abstract

LIGO employs two 4-km long Fabry–Pérot arm cavities, which need to be aligned in order for an interferometer to be locked on a TEM00 mode. Once the cavity is locked, alignment signals can be derived from wave-front sensors which measure the TEM01 mode content. However, the alignment state is not always good enough for locking on TEM00. Even when this is the case, the alignment can be evaluated using a free swinging cavity, that shows flashes when higher-order modes become resonant. By moving test masses, small changes are made to the mirror orientation, and hence the TEM00 mode can be optimised iteratively. Currently, this is a manual procedure, and thus it is very time-consuming. Therefore, this project is aimed to study another possible way to lock the cavity on the TEM00 mode. Misalignment information can also be extracted from the power of the higher-order modes transmitted through the cavity. This report presents an algorithm for this alternative and faster way to derive the alignment state of the arm cavities.

LIGO

University of Glasgow
VIA VERITAS VITA

Contents

1 Introduction **1**
1.1 LIGO . . . 1
1.2 Motivation and objectives . . . 1

2 Background theory **1**
2.1 Electric field . . . 1
2.2 Gaussian beam . . . 2
2.3 Hermite-Gaussian modes . . . 3
2.4 Gouy phase-shift . . . 3
2.5 Misalignments . . . 4

3 Experimental method **4**
3.1 Exposition . . . 4
3.2 Software . . . 5

4 Simulation **5**
4.1 Optical cavity . . . 5
4.2 Set-up . . . 6
4.3 Decomposition coefficients . . . 7

5 Algorithm **10**
5.1 Realistic simulation . . . 10
5.2 Set-up . . . 10
5.3 Development . . . 11
5.4 Testing . . . 13

6 Automation **14**
6.1 Data collection . . . 14
6.2 Region selection . . . 14
6.3 Data processing . . . 17
6.3.1 Anti-spike function . . . 17
6.3.2 Anti-resolution function . . . 17
6.3.3 Down-sampling . . . 19
6.4 Butterworth filter . . . 19
6.5 Results . . . 20

7 Conclusions **20**

A Mode Decomposition Coefficients **22**

B Code **22**

References **22**

1 Introduction

1.1 LIGO

LIGO stands for the Laser Interferometer Gravitational-Wave Observatory. There are two identical observatories based approximately 3,000 kilometres apart: one is in Livingston, Louisiana, and its twin is located at the Hanford site, Washington. The Hanford-site Observatory is the one where this project has been carried out. It is required that, if a signal is to be reliably defended as an astrophysical gravitational wave, it must be observed in both observatories. Gravitational-wave signals are so weak that gravitational wave detectors suffer a lot from background noise: strong earthquakes, or cultural noise such as traffic or trains, winds or microseism can negatively impact their performance. Many efforts are put into stabilising system to ensure that those effects are eliminated or reduced to minimum.

The Hanford-site detector is an interferometer which contains two 4 km-long arm cavities formed into "L" shape. The optical configuration of each detector is a suspended, dual-recycled Michelson interferometer with Fabry-Pérot cavities for arms. They need to be aligned, before they can be locked on a fundamental transverse mode, TEM00. Once the cavity is locked, or controlled on resonance, alignment signals can be derived from wave-front sensors which measure the TEM01 mode content, which is a superposition of Hermite-Gaussian TEM01 and TEM10 modes. However, the alignment state is not always good enough for locking on TEM00. Even when this is the case, the alignment can be evaluated using a free swinging cavity, that shows flashes when higher-order modes become resonant. This requires another round of optimisation, which is currently done manually.

1.2 Motivation and objectives

The goal of this project was to derive the alignment state from scanning the cavity length and observing the power build-up of the laser light. By making small changes to the mirror orientation by moving test masses, the TEM00 mode could be optimized iteratively. If the alignment state was derived from scanning the cavity length, this would ease the process of initial alignment. Another goal of the project was to automate the alignment procedure in order to reduce the manual alignment time, i.e. reduce the time to align a given cavity, and increase the reliability and repeatability in doing so.

2 Background theory

2.1 Electric field

An electric field, E, can be described as a sum of the different frequency components and of the different spatial modes:

$$E(t,x,y,z) = \sum_j \sum_{n,m} a_{jnm} u_{nm}(x,y,z) exp(i(\omega_j t - k_j z)),$$

with u_{nm} describing the spatial properties of the beam and a_{jnm} representing the complex amplitude factors. Here ω_j stands for the angular frequency, i.e. $\omega_j = 2\pi f_j$, and $k_j =$

ω_j/c defines the wave-number. This above notation can be simplified to describe a single frequency component at one moment in time ($t = 0$):

$$E(x, y, z) = exp(-ikz) \sum_{n,m} a_{nm} u_{nm}(x, y, z).$$

2.2 Gaussian beam

A simple laser beam can be described by the Gaussian beam to a good approximation. It can be divided into two different sections along the z-axis: a near field regime, which is a region around the beam waist, and a far field regime, which is a region far away from the waist. The length of the near-field region (Figure 1) is approximately given by the Rayleigh range,

$$z_R = \frac{\pi w_0^2}{\lambda},$$

where w_0 indicates the radius of the beam-waist and λ is the wavelength of the light beam.

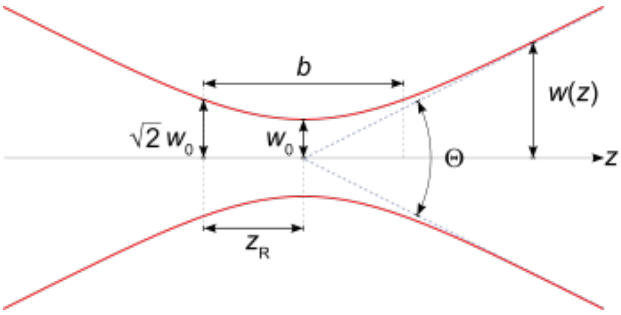

Figure 1: Gaussian beam.[1]

Knowing the Rayleigh range, z_R, and the location to the beam waist position, z_0, the following can be calculated:

$$w(z) = w_0 \sqrt{1 + \left(\frac{z - z_0}{z_R} \right)^2}.$$

This equation gives the size of the beam along the z-axis. In the far-field regime, where $z \gg z_R, z_0$, it can be approximated by a linear equation:

$$w(z) \approx w_0 \frac{z}{z_R} = \frac{z\lambda}{\pi w_0}.$$

The angle θ between the z-axis and $w(z)$ is called the diffraction angle, or divergence, and in the far-field regime, it is defined as:

$$\theta = \arctan\left(\frac{w_0}{z_R} \right) = \arctan\left(\frac{\lambda}{\pi w_0} \right) \approx \frac{w_0}{z_R}.$$

2.3 Hermite-Gaussian modes

Hermite-Gaussian modes are the eigenmodes of a general spherical cavity (an optical cavity with spherical mirrors) that represent an exact solution of the paraxial-wave equation. One distinguishes between longitudinal modes (along the optical axis) and transverse electromagnetic modes (TEM), which are the spatial distribution of the light beam perpendicular to the optical axis. The higher-order Hermite-Gaussian mode can be expressed in terms of the lowest-order, or fundamental, mode, u_{00}, which is simply the Gaussian beam:

$$E(x,y,z) = E_0 u_{00} exp(-ikz) = E_0 \left(\frac{1}{R_c(z)} - i\frac{\lambda}{\pi\omega^2(z)} \right) \times exp\left(-ik\frac{x^2+y^2}{2R_C(z)} - \frac{x^2+y^2}{\omega^2(z)} - ikz \right)$$

(assuming a single frequency and $t = 0$). Here E_0 is the electric field of TEM00 mode, $R_C(z)$ is the radius of curvature of the beam's wave-front, and x, y, and z denote three spatial directions orthogonal to each other.

The Hermite-Gaussian modes are usually given in their orthonormal form as:

$$u_{nm}(x,y,z) = (2^{n+m+1} n!m!\pi)^{-1/2} \frac{1}{w(z)} exp(i(n+m+1)\Phi(z)) \times H_n\left(\frac{\sqrt{2}x}{w(z)}\right) H_m\left(\frac{\sqrt{2}y}{w(z)}\right) exp\left(-i\frac{k(x^2+y^2)}{2R_C(z)} - \frac{x^2+y^2}{w^2(z)} \right),$$

with n, m being the mode indices. In this case n refers to the modes in the $y-z$, or saggital, plane and m to the modes in the $x-z$, or tangential, plane. In the equation above, $H_n(x)$ stands for the Hermite polynomials of the order n and $\Phi(z)$ is the Gouy phase.

2.4 Gouy phase-shift

Compared to a plane wave, the Hermite-Gaussian modes have a slightly slower phase velocity, especially close to the waist, in the near-field region. This on-axis longitudinal phase delay is called the Gouy phase:

$$\Phi(z) = \arctan\left(\frac{z-z_0}{z_R}\right).$$

The phase lag ϕ of a Hermite-Gaussian mode is:

$$\phi = (n+m+1)\Phi(z),$$

which is called the Gouy phase-shift. It is an additional phase shift of π in addition to $exp(-ikz)$, the usual phase shift for a plane wave. This additional phase shift appears due to the fact that a Gaussian beam passes the beam waist when travelling from the far-field regime on the left to the beam waist to the other far-field regime on the right to the beam waist, or vice versa.

2.5 Misalignments

In the interferometer, if the optical axes of the beam and the cavity do not overlap perfectly, the set-up is called misaligned. If the beam size or shape at the cavity does not match the beam size and shape of the (resonant) fundamental eigenmode, the beam is then not mode-matched to the cavity.[2] There are four possible types of misalignments of the input axis with respect to the cavity axis: (a) waist size mismatch, (b) axial waist displacement, (c) transverse displacement in the $x(y)$-direction, and (d) tilt through an angle $a_x(a_y)$.[3]

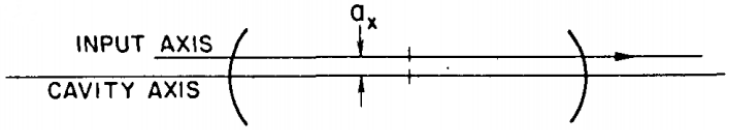

Figure 2: Example of misalignment: transverse displacement.[3]

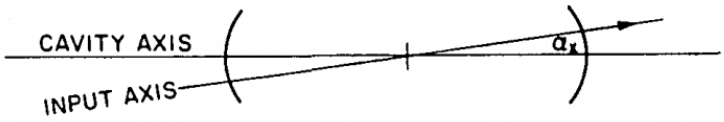

Figure 3: Example of misalignment: tilt through an angle α.[3]

Example plots of two types of misalignment are pictured above. Figure 2 shows the transverse displacement and Figure 3 shows the misalignment due to the mirror tilt.

3 Experimental method

3.1 Exposition

In order to develop an algorithm, the work was split into smaller tasks. The first part of the project was to understand modal decomposition coefficients. This was done using MATLAB programming language[4] and a software package called FINESSE.[5] In the initial simulation, a simplified cavity was used, which was later adapted to match the realistic parameters. The output of this simulation part was a modal decomposition coefficient table and their ratio table. The first one is shown in Table 3.

The second part of the project was the algorithm development. To create an output product, Gouy phase shift and Gaussian geometry were used together with various statistical techniques. The outcome of this part was an algorithm, which reads in the power-distribution data, finds the peak values and their positions, takes the ratios of the peak amplitudes with respect to the highest peak, reorders the amplitudes according to their

relative positions, and after a procedure of matching to the values from the ratio table from the simulation part, extracts the normalised misalignment parameter. After the algorithm was developed, further tests were done to improve it and to test its limits of validity.

The algorithm was created using the simulated-data input. Therefore, the objective of the last part of the project was to adapt the algorithm to the real-data input from the interferometer. The seven sets of data were collected at the LHO (LIGO Hanford site) X-arm. In order to make the algorithm work, only one region corresponding to a single-trip of data needed to be selected. Since the systematic calibration did not work perfectly, other methods were used to define the data in the required region of fringe scan. The peak-finding algorithm also needed to be robuster, therefore, such functions as "anti-resolution" or "anti-spike" were introduced. And finally, because the collected data were rough, some data preparation methods such as interpolation and down-sampling were used and a digital low-pass Butterworth filter was applied.

3.2 Software

An important initial step for this project was to choose the right software for the simulation of modal decomposition coefficients. Two software packages, FINESSE[5] and E2E,[6] were considered. FINESSE was selected due to its ability to perform calculations for the higher-order Hermite-Gaussian modes, because its competitor E2E[6] could only offer the calculations for the fundamental mode HG_{00}. Thus, a lot of from-scratch programming was avoided. To invoke FINESSE scripts and to produce graphical output, a programming language was necessary. For this purpose, MATLAB was chosen. MATLAB also has a signal-processing toolbox, which has made the analysis of the real data from the interferometer easier to deal with.

4 Simulation

4.1 Optical cavity

The starting point for the project was a cavity simulation. Using FINESSE software package,[5] green TEM00 laser light (532 nm) was injected into the optical system from the end point, i.e. we simulated green light injection from downstream of the end mass, into the cavity and back towards the input test mass (ITM) in the corner station. End test mass (ETM) transmitted 32% of the initial beam further to the input test mass. As only 1.1% of the beam passed through the ITM, most of the beam remained inside the cavity and was reflected back and forward multiple times. In a perfectly aligned system, the output beam should have the same transverse mode as the input beam. However, even minimal misalignments of the optics could cause the higher-order Hermite-Gaussian modes to appear. In order to develop an algorithm to minimise the appearance of the higher-order Hermite-Gaussian modes, a simulation of a misaligned system was modelled.

Since the laser beam could be approximated as a Gaussian beam, the initial step was to calculate the beam-waist radius and the distance to the beam waist for a simple cavity with two mirrors with unequal curvatures. The set-up of this simplified cavity is displayed in Figure 4. Using the formula for confocal parameter, b, and its relation to the beam-waist

radius, w_o,

$$\frac{1}{2}b = \frac{\pi w_0^2}{\lambda} = \frac{\sqrt{d(R_1-d)(R_2-d)(R_1+R_2-d)}}{R_1+R_2-2d},$$

$$w_0 = \sqrt{\frac{\lambda}{\pi}}\frac{\sqrt[4]{d(R_1-d)(R_2-d)(R_1+R_2-d)}}{\sqrt{R_1+R_2-2d}},$$

the beam-waist radius was estimated to be $w_0 = 8.47$ mm. Another equation from Kogelnik's paper[7] enabled us to calculate a distance to the beam-waist radius,

$$t = \frac{d(R_2-d)}{R_1+R_2-2d}.$$

Here $R_2 = 1939.3$ m and $R_1 = 2241.54$ m are the radii of curvature for the ITM and ETM respectively, and $d = 4000.0$ m is the length of the interferometer arm, i.e. the length of the cavity. In this particular set-up, this was the distance between the ETM and the beam-waist radius, which was found to be $t = 1841.72$ m.

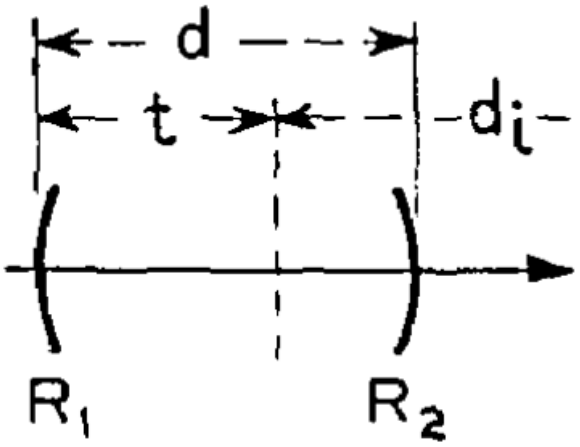

Figure 4: Optical system with two mirrors.[7]

4.2 Set-up

An example set-up that was used to study modal decomposition coefficients could be found in Figure 5. Laser was set to emit 1 W green ($\lambda = 532$ nm) light. In this particular simulation, only one totally-reflective ITM mirror was used; it was described by the parameter L, the distance between the laser and the ITM. The amplitude detector was placed between the laser and the mirror. It plotted the light field at the specified frequency, whose amplitudes were in good agreement with the pre-calculated values. The amplitude at frequency ω_m is a complex number (z), and is calculated as follows:

$$z = \sum_n a_n \text{ with } n | n \in 0, \ldots, N \wedge \omega_n = \omega_m.$$

Here ω_0 is the carrier frequency and $\omega_1, \omega_2, \cdots, \omega_M > 0$ are the sidebands. The result can be written as follows:

$$S = a \exp(i\Phi),$$

with

$$a = \sqrt{\sum_{n,m} |a_{n,m}|^2} \text{ and } \Phi = \text{phase}\left(\sum_{n,m} a_{n,m}\right).$$

To check the intensity, which should be proportional to the square of an amplitude,

$$I \propto a^2 \propto |E|^2,$$

the photo-detector was placed to the right of the ITM mirror. The intensity at the output port of the photo-detector was found from

$$|E|^2 = E \times E^* = \sum_{i=0}^{N} \sum_{j=0}^{N} a_i a_j^* e^{i(\omega_i - \omega_j)t} = A_0 + A_1 e^{i\overline{\omega_1}t} + A_2 e^{i\overline{\omega_2}t} + \cdots,$$

with A_i being the amplitudes of the light power sorted by the beat frequencies $\overline{\omega_i}$.

By default, the plane-wave approximation was used in FINESSE simulation. The order of the higher-order modes was finite and it was defined by the parameter `maxTEM`. The simulation included higher-order modes TEM_{nm} with $n + m \leq$ `maxTEM` order.

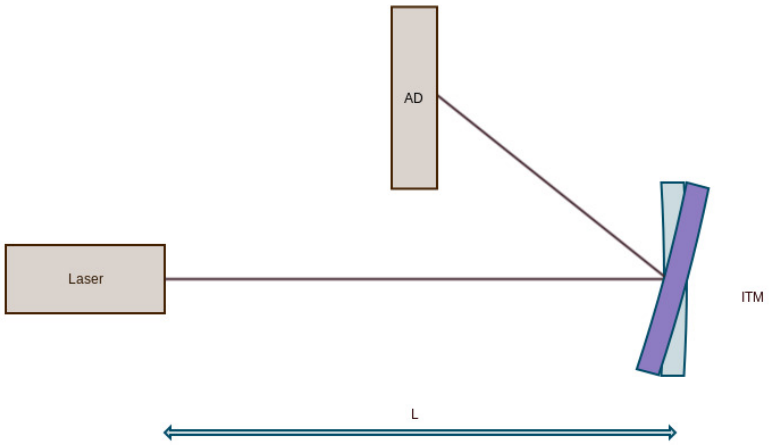

Figure 5: Simulation set-up.

4.3 Decomposition coefficients

HG_{00} mode is a combination of higher-order Hermite-Gaussian modes, where U_{mn} defines the mode and a_{mn} is a modal amplitude factor,

$$U_{00}(x, y, z) = \sum_{m,n} U_{mn}(x', y', z') a_{mn}.$$

Therefore, the first milestone of the project was to study decomposition coefficients, a_{mn}. Initial simulation was written to calculate those coefficients for a light reflected from a flat mirror located at the beam waist. The motive to use this particular set-up for an initial simulation was based on FINESSE limitations.

Because of the geometry of the reflection law, when a flat mirror was located at the beam waist, the total angle of misalignment was $\alpha = 2\theta$, where θ stood for a tilt angle of the mirror. A plot showing the distribution of the first six TEM modes is shown in Figure 6. Later, the mirror was moved along the z-axis and its curvature was iterated correspondingly to match the wave-front of the beam, i.e. the distance to the mirror, L, was changed from $L = t$, which was the distance to the beam waist, to $L \approx 10t$.

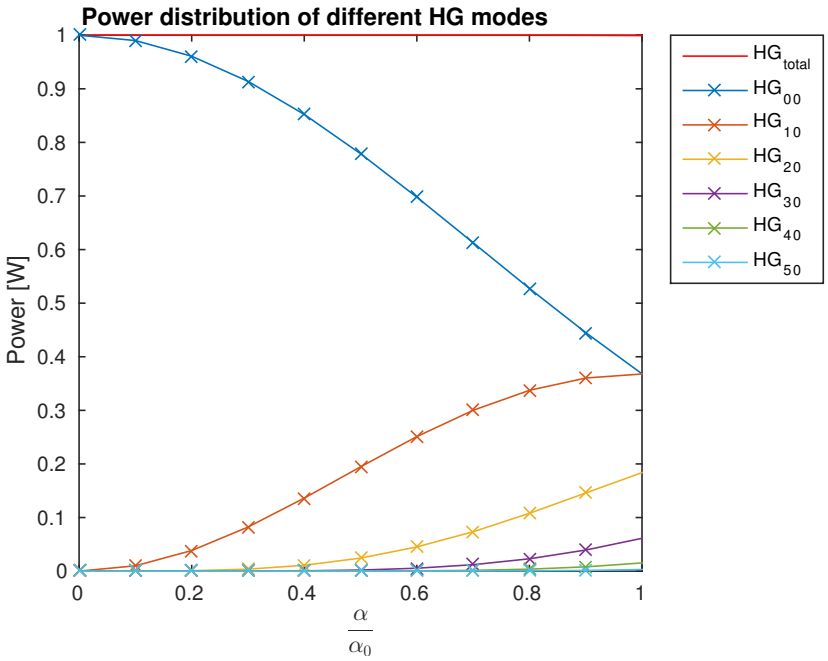

Figure 6: Reflected power distribution of the first six TEM modes for various mirror misalignments $\frac{\alpha}{\alpha_0}$.

The x-axis of the plot was a misalignment parameter,

$$\left| i\frac{\alpha}{\alpha_0} + \frac{a}{w_0} \right|.$$

Since the radius of the curvature of the mirror was matched to the displacement along the z-axis, i.e. $\frac{a}{w_0}$ became 0, the misalignment parameter simplified to $\left| i\frac{\alpha}{\alpha_0} \right|$.

For R_{ETM} and R_{ITM}, radii of curvatures of the ETM and of the ITM, the misalignment angle α can be rewritten as

$$\alpha = \frac{R_{ETM}\theta_{ETM} + R_{ITM}\theta_{ITM}}{R_{ETM}R_{ITM} - L},$$

where α_0 is a divergence angle,

$$\alpha_0 = \sqrt{\frac{\lambda}{\pi}} \sqrt[4]{\frac{(R_{ETM} + R_{ITM} - 2L)^2}{L(R_{ETM} - L)(R_{ITM} - L)(R_{ETM} + R_{ITM} - L)}},$$

a is a tilt, and w_0,

$$w_0 = \sqrt{\frac{\lambda}{\pi}} \sqrt[4]{\frac{L(R_{ETM} - L)(R_{ITM} - L)(R_{ETM} + R_{ITM} - L)}{(R_{ETM} + R_{ITM} - 2L)^2}}$$

is the beam-waist radius. Using the approximations

$$tan(\alpha) \approx \alpha \text{ for a small } \alpha,$$

and

$$\text{when } R_{ITM} \to \infty, \ \frac{R_{ITM} + R_{ETM} - 2L}{R_{ITM} - L} \times \frac{R_{ITM} + R_{ETM} - 2L}{R_{ITM} + R_{ETM} - L} \to 1,$$

the divergence angle becomes

$$\alpha_0 = \sqrt{\frac{\lambda}{\pi}} \sqrt[4]{\frac{1}{L(R_{ETM} - L)}},$$

and the above equation for the x-axis can be derived.

In order for the optical element (ITM mirror in this case) to match the wave-front of the beam, its shape had to be corrected accordingly. Since the location of the mirror was iterated along the z-axis, the radius of its curvature was also iterated:

$$R(L) = L\Big[2 + \Big(\frac{\pi w_0^2}{\lambda L}\Big)\Big].$$

Furthermore, in order to compare the plots for different L, the x-axis was normalised using the normalisation constant, θ_C,

$$\theta_C = \sqrt{1 + \Big(\frac{\alpha_0}{w_0}\Big)^2 (L^2 - (2{\times}L{\times}t) + (t)^2))},$$

where the variables had their usual meanings defined previously.

The power distribution plot is shown in Figure 7. This shows only negligible differences for the mirror placed at different positions, which means that the normalisation has been done correctly. The results of the obtained decomposition coefficients, a_{mn}, for the first 11 higher-order modes (HOM) are laid out in Table 3. The table can be expanded horizontally by including more HOM and vertically by increasing the value of the maximal tilting angle.

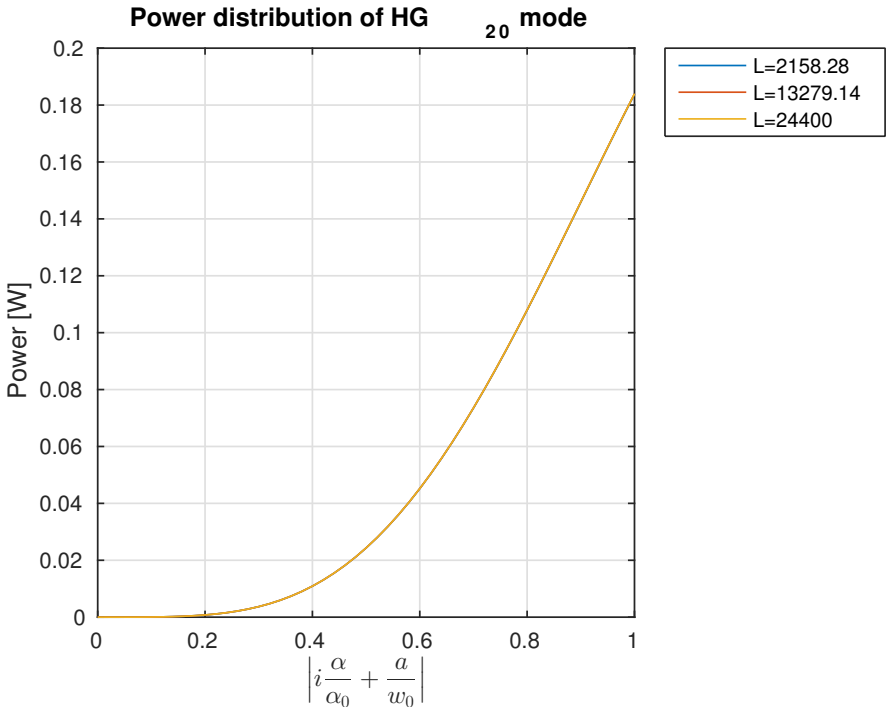

Figure 7: Power distribution of HG_{20} mode for different mirror positions along the z-axis; x-axis normalised.

5 Algorithm

5.1 Realistic simulation

The second step started with a simulation that used realistic parameters. An original set-up from the first part was taken as a basis, which was adjusted to reflect realistic characteristics of the cavity. Both of the mirrors, ETM and ITM, were incorporated and the cavity length was set to the actual value used at LIGO. In this realistic case, mirrors were being tilted at various angles, and the output power was studied for several combinations of tilt angles and a different number of TEM modes. A $3-D$ plot of the power distribution of HG_{20} mode is shown in Figure 8.

5.2 Set-up

For the realistic simulation, the input was expected to be in the form of a power distribution at a given position along the interferometer arm. The algorithm should then compare the amplitudes of the power peaks and the relative peak heights and should output the misalignment parameter,

$$\mathcal{O}\left[\left(\frac{a}{w_0}\right)^2+\left(\frac{\alpha}{\alpha_0}\right)^2\right].$$

The biggest challenge of this part of the project was the extraction of the misalignment information. This was achieved in stages. The first stage, later called $1-D$ case, only looked at the tilt of one mirror, i.e. if $\alpha_{ITM}\neq 0$ then $\alpha_{ETM}=0$, and vice versa. The

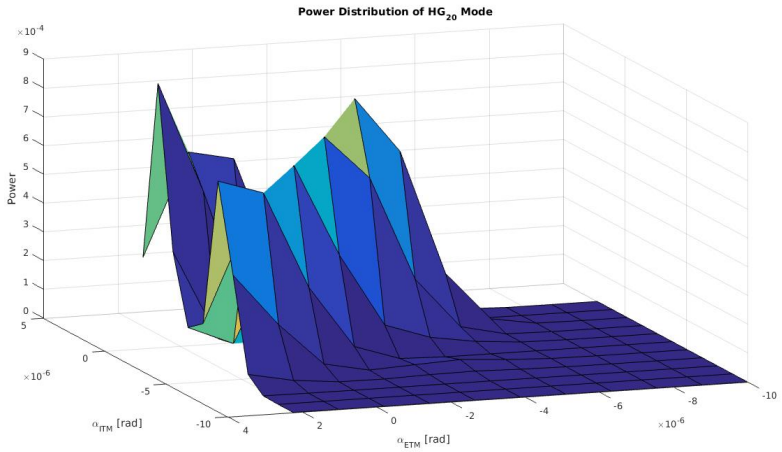

Figure 8: $3-D$ power distribution of HG_{20} mode after misaligning both mirrors.

next stage, so called $2-D$ case, introduced four angles: both ETM and ITM were allowed to move in two directions making pit and yaw rotations. However, if the pit angles were chosen freely, yaw angles for both ETM and ITM were restricted. The restrictions were defined by the relations below, so that one plane would show only transverse displacement, whilst the other plane (perpendicular to the first one) would show the tilt through an angle α. Similar restrictions were applied to the pit angles when yaw angles were chosen freely.

$$\frac{\alpha_Y}{\alpha_0} = \frac{R_{ETM} \cdot \alpha_{ETM} + R_{ITM} \cdot \alpha_{ITM}}{(R_{ETM} + R_{ITM} - L) \times \alpha_0},$$

$$\frac{\alpha_P}{\alpha_0} = \frac{R_{ETM} \cdot \alpha_{ETM} - R_{ITM} \cdot \alpha_{ITM}}{(R_{ETM} + R_{ITM} - L) \times \alpha_0},$$

$$\frac{a}{\omega_0} = \frac{(R_{ETM} - t) \times (R_{ITM} \cdot \alpha_{ITM}) - (t - L + R_{ITM}) \times (R_{ETM} \cdot \alpha_{ETM})}{(R_{ITM} + R_{ETM} - L) \times \omega_0},$$

where indices $_P$ and $_Y$ stand for the pit and yaw respectively. And finally, the $3-D$ case corresponded to the case, where both pit- and yaw-angles for both ETM and ITM were chosen arbitrarily.

The set-up for this part of the simulation is shown in Figure 9. Here L represents the cavity length, t is the distance to the beam waist, $R_{C_{ETM}} = 2241.54$ m and $R_{C_{ITM}} = 1939.3$ m are the radii of the curvatures of the ETM and ITM.

5.3 Development

The idea of the algorithm was to match the peaks found from the fringe scanning to the modal decomposition coefficient data obtained in the first part of the project and to extract the information about the normalised misalignment parameter. In order to do that, the peaks needed to be correctly reordered.

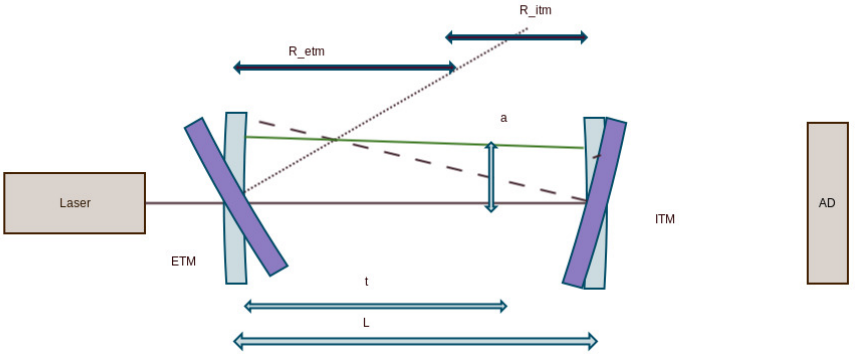

Figure 9: Realistic cavity set-up.

One of the methods to reorder the input peaks and to match them to the higher-order HG modes was to use the Gouy phase. The Gouy phase change was evaluated for all TEM modes considered in the simulation, and the relative peak positions were determined using

$$\Phi(m,n;L) = (m+n+1)\arctan(\lambda L/\pi w_0^2),$$

where (m,n) were the indices of the Hermite-Gaussian modes. Therefore, the field amplitude u became:

$$u_{m,n}(r,z) = \frac{w_0}{w} \times H_m\Big(\sqrt{2}\frac{x}{w}\Big)H_n\Big(\sqrt{2}\frac{y}{w}\Big)$$
$$\times exp\Big\{ -i(kz-(m+n+1)\Phi) - r^2\Big(\frac{1}{w^2}+\frac{ik}{2R}\Big)\Big\}.$$

Also, for identification of the misalignment parameters, Table 3 was used as a reference table.

The algorithm logic was quite simple. Firstly, the peaks and their locations were found, as shown in Figure 10 and Figure 11. A vector containing peak amplitudes was called PKS and another one containing peak locations - LOCS. Then for each row, the ratios with regard to the highest peak were taken. The peak-ratio vector was called PKR. When this was done, the re-ordering process began at the PKR element whose value was equal to 1, PKR_i. A pre-calculated Gouy phase-shift was added to the right of the LOC_i and to the left. The direction 'to the right' meant that the Gouy phase-shift was added to the LOC_i and then the modulus operation `mod` 180 was applied, and 'to the left' meant that the Gouy phase-shift was subtracted from the LOC_i, following with a subsequent modulus operation, `mod` 180. After that, two new locations were obtained, LOC_{L2R} and LOC_{R2L}. The minimisation function was used to find the closest element to each of them in the PKR vector: LOC'_{L2R} and LOC'_{R2L}. When those elements were found, the distances between LOC_{L2R} and LOC'_{L2R} and between LOC_{R2L} and LOC'_{R2L} were compared and the shortest one was kept. If the shortest distance was 'to the left', i.e.

$$\Delta(LOC_{R2L} - LOC'_{R2L}) < \Delta(LOC_{L2R} - LOC'_{L2R}),$$

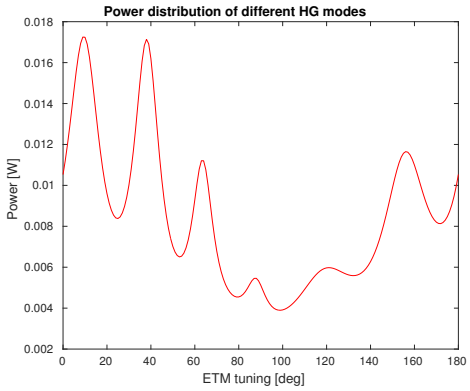

Figure 10: Simulated peaks.

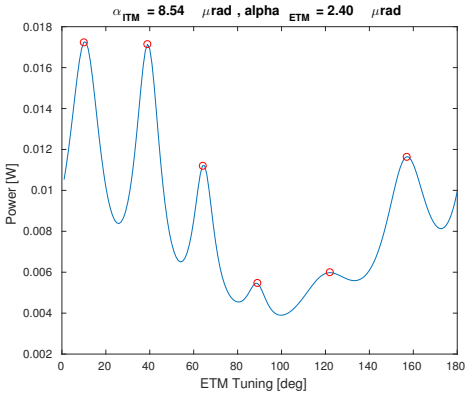

Figure 11: *findpeaks* finds peaks and their locations.

then the PKR_i corresponding to the location LOC_{R2L} was added to the maximum PKR_i (or $GOUY\_PKR_i$) on the left side, otherwise - on the right side. The new vector that was being filled was called $GOUY\_PKR$. The elements that had been assigned to the $GOUY\_PKR$ were deleted from the remaining list of PKR items, so that the re-ordered values would not be repeated. The same shortest-distance procedure was repeated for the edge-most elements of the new $GOUY\_PKR$ vector until the original PKR vector was empty and until the $GOUY\_PKR$ had the same length as the PKR vector before the re-ordering procedure. Figure 12 and Figures 13, 14, 15 show the re-ordering procedure.

5.4 Testing

The algorithm was tested using three sets of `maxTEM` = 15, 20, and 25. It was also tested for all three cases considered previously: $1-D$, $2-D$, and $3-D$. The plots in Figures 16, 17, 18, and 19 show the limitations for the algorithm to extract the correct misalignment parameter. As can be seen from the graphs, the algorithm works best when describing the normalised misalignment in the region where the values of the misalignment are equal to 0.5 - 2.0. It is hypothesised that the algorithm does not work when the misalignment is very big because the paraxial approximation does not hold any more.

Another sanity check used as a test was a transmittance plot. Transmittance was calculated using a formula,

$$T(\Phi) = T_1 T_2 \frac{1}{|1 - r_1 r_2 e^{0i\Phi}|^2} = \begin{cases} \Phi = 0, \frac{T_1 T_2}{(1-r_1 r_2)^2}, \\ \Phi = \pi, \frac{T_1 T_2}{(1+r_1 r_2)^2}, \end{cases}$$

with r_1 and r_2 being the amplitudes.

$$T_{combined} = P_0 T(\Phi) + P_1 T(\Phi + Gouy) + P_2 T(\Phi + 2 \cdot Gouy) + \cdots + P_{n+m} T(\Phi + (n+m) \cdot Gouy),$$

where *Gouy* meant the Gouy phase shift. If two plots, one obtained using the FINESSE software and the other one from the pre-calculated transmittance, were completely different, then those cases were assumed as FINESSE failures and were rejected from the

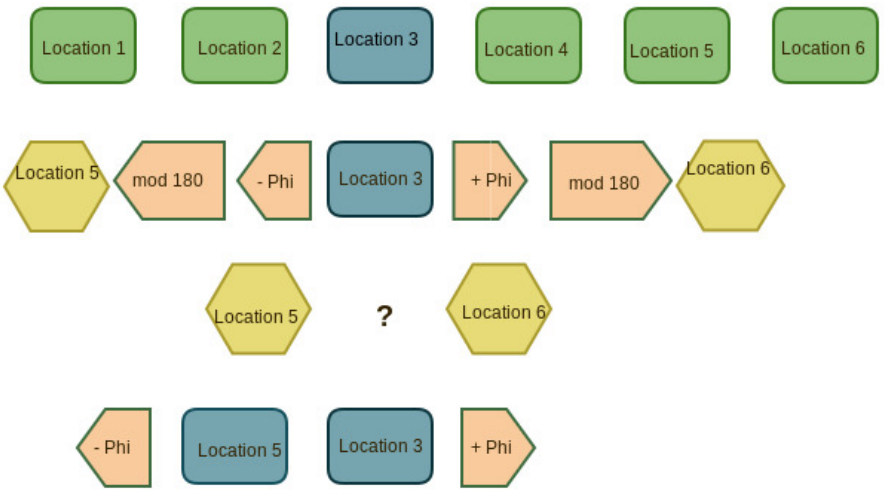

Figure 12: Scheme of the PKR re-ordering. A question mark identifies a step, where the distances to the two candidate elements are being compared resulting in the closest element being assigned to the $GOUY\_PKR$.

calculation. They would usually correspond to the cases where the combined misalignment parameter was very large. Figure 20 shows a good agreement between a FINESSE power distribution and a pre-calculated power.

6 Automation

6.1 Data collection

Seven measurements of channel H1_SUS_ETMX_L1_LOCK_L_EXC were taken, which were later used to adapt the algorithm to the real data entry. The gain that was used was 3×10^6 with a time of 5 s, Dt equal to 1, and a frequency of 1 Hz. Values calculated from the relative displacements were regarded as the normalised true misalignment parameter, and a deviation between the true and estimated values was obtained at each sample point. Results are shown in Table 1.

6.2 Region selection

Calibration of the optical cavity could be evaluated using the information from the witness sensors,

$$\frac{|Witness_{TO} - Witness_{FROM}|}{\lambda} \times 360^o \approx 270^o.$$

For a green light, $\lambda = 532$ nm, LHO calibration gave 270^0 instead of the expected 180^o. Therefore, a new method to select the region of interest without using false calibration was

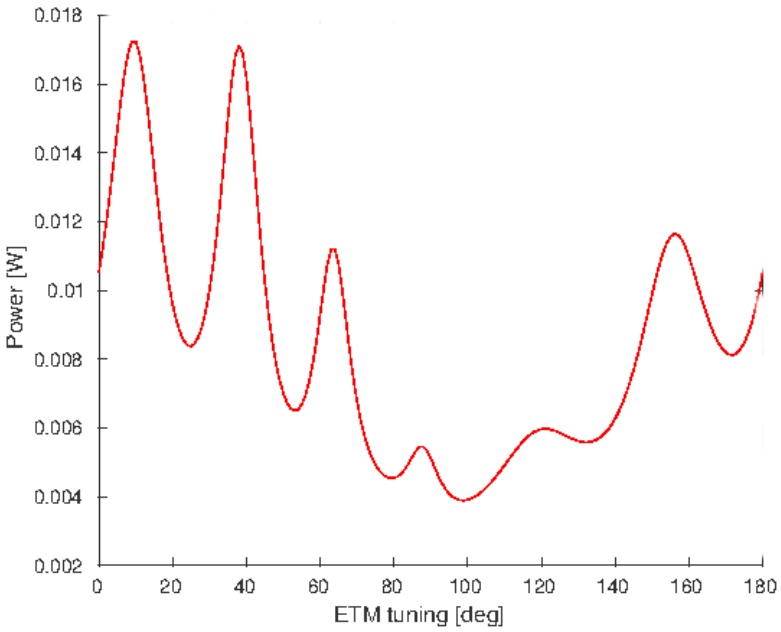

Figure 13: Re-ordering scheme: peak selection.

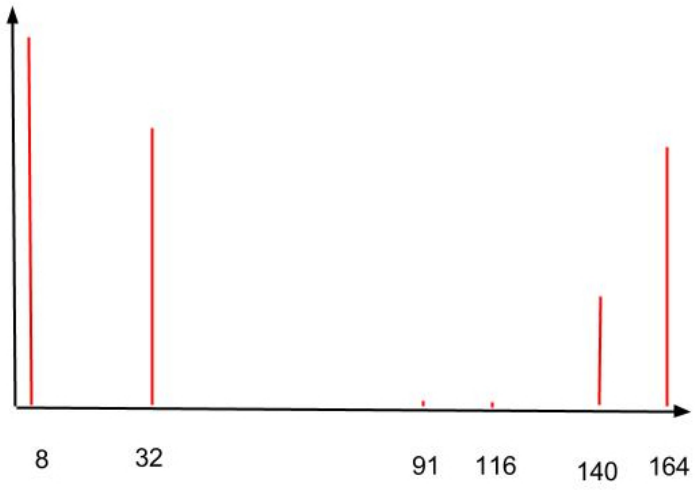

Figure 14: Vectors of peak ratios and their locations, PKR and LOCS.

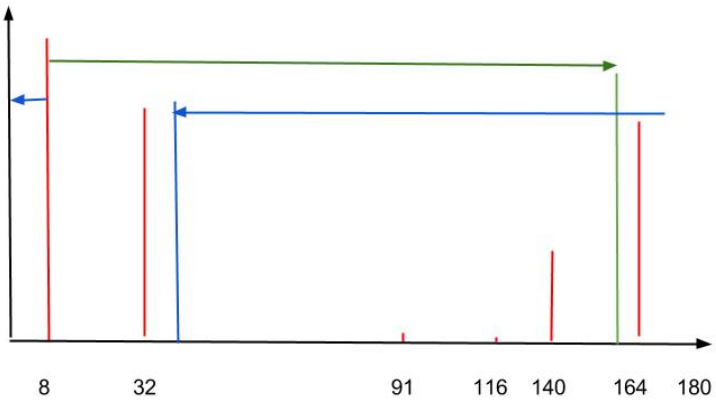

Figure 15: Filling the GOUY_PKR.

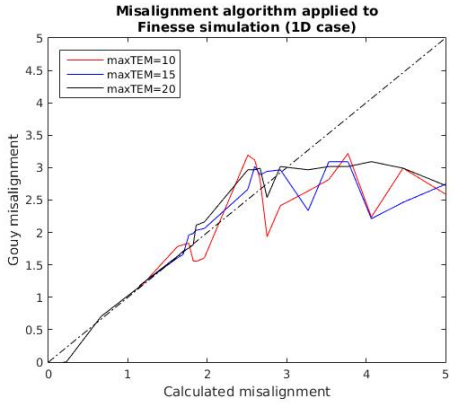

Figure 16: Algorithm testing: 1-D case, maxTEM = 15, 20, 25.

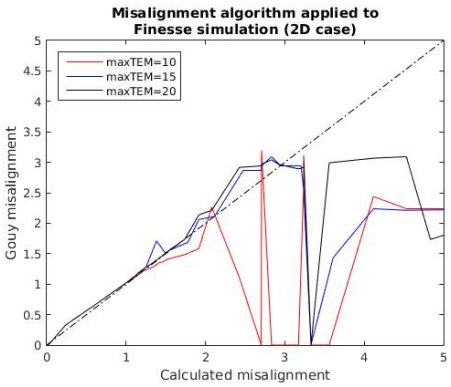

Figure 17: Algorithm testing: 2-D case, maxTEM = 15, 20, 25.

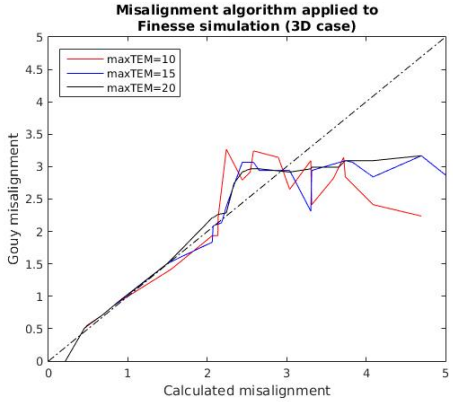

Figure 18: Algorithm testing: 3-D case, maxTEM = 15, 20, 25.

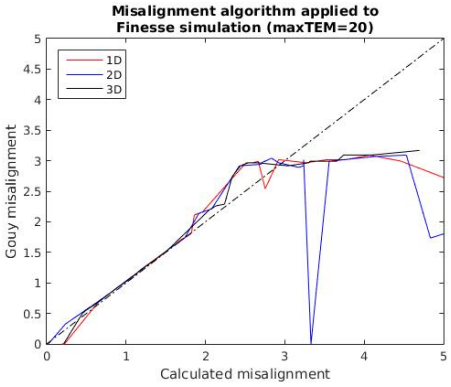

Figure 19: Algorithm testing: maxTEM = 20, 1-D, 2-D, 3-D cases.

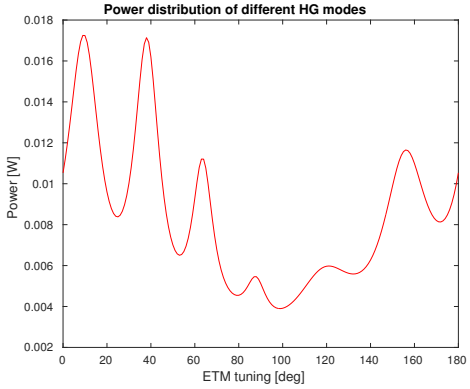

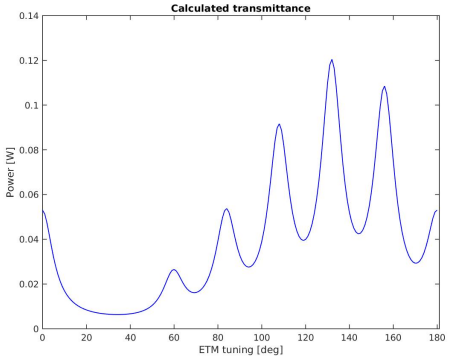

Figure 20: Power calculated with FINESSE and pre-calculated power shows good agreement.

invented. Power distribution was plotted against the information from the witness sensor and the maximal peak was found. Then by using the Gouy phase-shift, the second highest peak was also found in the region where the output from witness sensor was linear, i.e. cavity movement was constant, and the direction did not change (Figure 21). This allowed us to select a single-trip region of interest covering $\approx 180^o$.

No.	α_{ITM_P}	α_{ITM_Y}	α_{ETM_P}	α_{ETM_Y}	$\Delta\alpha_{ITM\_P}$	$\Delta\alpha_{ITM\_Y}$	$\Delta\alpha_{ETM\_P}$	$\Delta\alpha_{ETM_Y}$	Normalised true misalignment parameter
1	-78.7	1.7	4.8	80.3	0.0	0.0	0.0	0.0	0.000000
2	-76.5	-1.3	6.7	82.5	2.0	-3.0	1.9	2.2	0.687242
3	-74.8	-1.3	8.1	83.6	3.9	-3.0	3.3	3.3	0.903745
4	-74.8	0.0	7.2	81.3	3.9	-1.7	2.4	1.0	0.747380
5	-72.2	-0.3	9.2	81.9	6.5	-2.0	4.4	-8.4	6.405156
6	-70.2	0.4	10.4	81.4	8.5	-1.3	5.6	1.1	1.130984
7	-72.6	3.3	9.5	80.3	6.1	1.6	4.7	0.0	0.945770

Table 1: Green Transmission Measurements.

6.3 Data processing

Rough data collected in the last part of the project had a lot of small spikes and multiple peaks in close proximity to each other making it difficult to distinguish the "true" peaks. Thus, to use the algorithm, a manual selection of the region of interest was required. In order to avoid that, various techniques were used to process the data so that it could be used in an automated version of the algorithm.

6.3.1 Anti-spike function

An anti-spike function calculated the prominence of each peak and its true height. If the peak height was below the selected height (which was 60% from the highest peak in our case), it was instantly discarded from further considerations. If it was above the selected height, it was further analysed as a potentially "important" peak. The anti-spike function was introduced to eliminate little spikes that appeared because the cavity was shaking when the measurements were being taken, and/or because of the difference in the data taking frequency. Due to some hardware issues, an expected 8 kHz data was actually 2 kHz data and this was also a reason to introduce a down-sampling technique (Section 6.3.2).

6.3.2 Anti-resolution function

An anti-resolution function eliminated multiple "false" peaks, which appeared due to the shakiness of the cavity, i.e. the function "reduced" the resolution of the power distribution. The peaks in the region of interest were being scanned from left to right and then from right to left. While scanning, the function was checking whether a neighbouring peak to the peak that was being analysed was within a specified distance, which was set to 10% of the analysed peak height and which could be freely modified according to the smoothness of the dataset. In case there was a neighbouring peak within such distance, the height

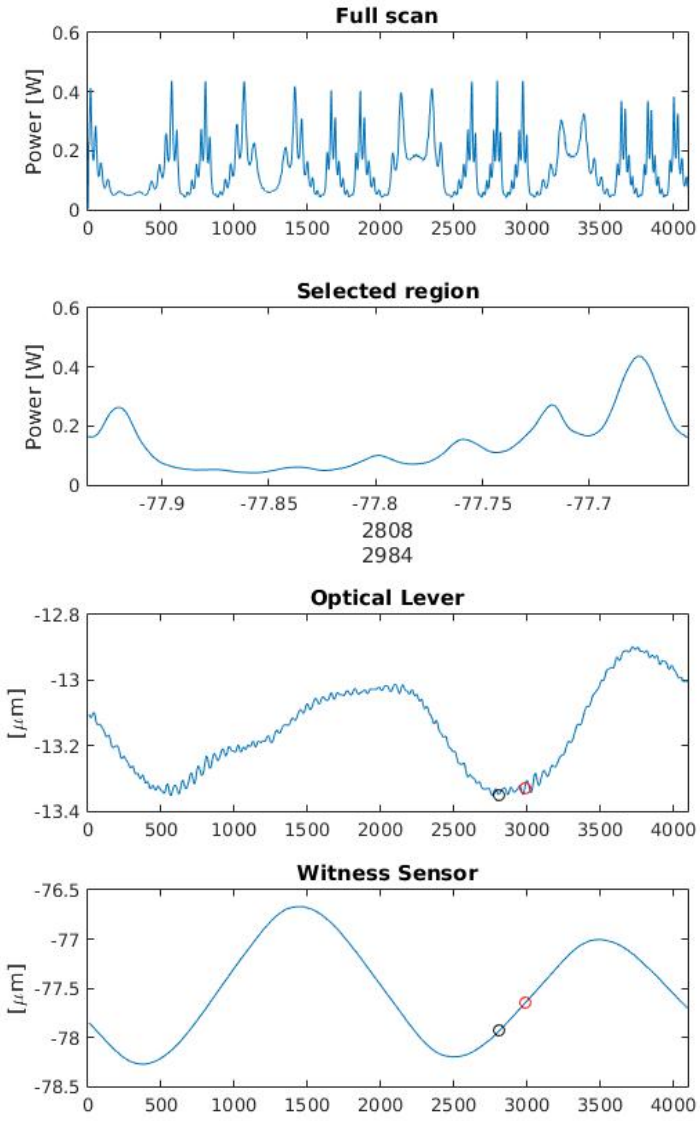

Figure 21: Region selection using the linearity of the witness sensor.

of the neighbouring peak and its prominence were compared to the peak that was being analysed. Then using these two criteria, one of the peaks was remained as a "true" peak and the other one was discarded as a "false" peak. In case two peaks were "twins", i.e. if they had exactly the same parameters, the neighbouring peak was regarded as a "false" peak. When a left-to-right scan was completed, the process was repeated towards the other side, i.e. a right-to-left scan was performed considering the remaining peaks only. On average, depending on the quality of the collected data, this function would eliminate 1 or 2 "false" peaks.

6.3.3 Down-sampling

Due to the hardware issue described previously, the measured dataset had four identical copies of each datum. Therefore, a down-sampling method was applied - every n^{th} data point was kept only. In our case, n was 4. To down-sample data, a linear interpolation method was used,

$$\frac{y - y_a}{y_b - y_a} = \frac{x - x_a}{x - x_b},$$

$$y = y_a + (y_b - y_a)\frac{x - x_a}{x_b - x_a}.$$

Knowing the values y_a and y_b, at points x_a and x_b respectively, a proportionality relation was used to estimate the value y of the point located at the position x.

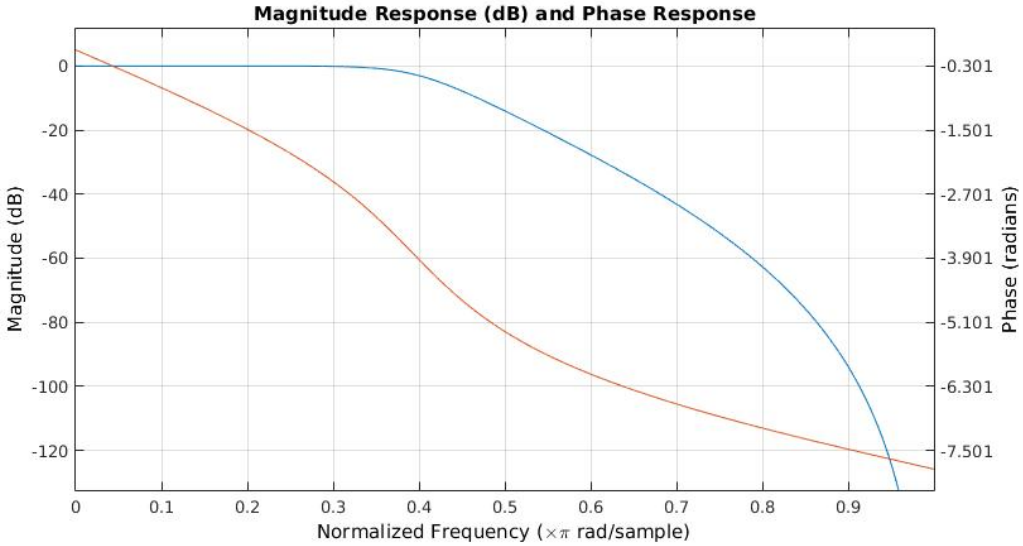

Figure 22: Digital low-pass Butterworth filter with $f_C = 400Hz$, $n = 5$.

6.4 Butterworth filter

A low-pass digital Butterworth filter was used to reduce a number of spikes in the collected data samples and to allow a more accurate selection of peaks and their locations.

The gain, $G(\omega)$, of such filter of an n^{th}-order could be expressed as

$$G^2(\omega) = |H(j\omega)|^2 - \frac{G_0^2}{1 + \left(\frac{\omega}{\omega_c}\right)^{2n}},$$

with $H(j\omega)$ denoting a transfer function, G_0 being a gain at 0 frequency, or DC gain, and $\omega_c = 2\pi f_c$ standing for the cutoff frequency. Figure 22 shows the Butterworth filter which was applied in our case.

6.5 Results

The algorithm was tested with seven datasets collected at LHO interferometer. The results are displayed in Table 2. The upper line stands for a theoretically pre-calculated misalignment, or "true" misalignment, while the lower line shows the misalignment parameter returned by the algorithm.

#	1	2	3	4	5	6	7
True	0	0.687242	0.903745	0.747380	6.4055156	1.130984	0.945770
Algorithm	0.4220	0.8158	1.2096	0.6470	2.8131	0.9002	0.9283

Table 2: Evaluation of the algorithm for seven datasets.

Results confirm that the algorithm extracts the misalignment parameter as expected in the range between 0.68 and 1.13. The returned misalignment value for the case with no misalignment, i.e. for the dataset #1, lies within a reasonable level of uncertainty. However, the algorithm has failed to extract the normalised misalignment parameter for a dataset #5. There are two possible reasons to explain why this has happened. Firstly, the "true misalignment" was out of the "good-performance" range (Section 5.4). And secondly, the validity of the dataset #5 was questionable. An information given from a witness sensor was used to examine each of the datasets. There were some clues that the data in the dataset #5 was collected when a cavity was in a non-linear regime, and thus it should be rejected.

7 Conclusions

The algorithm developed during this project can accurately extract the information about the normalised misalignment parameter within a range between 0.5 and 2.0. During the development stage, two new functions for more robuster peak selection were created. An "anti-resolution" function eliminates peaks that are too close together and an "anti-spike" function uses prominence to separate real peaks ("true" peaks) from the accidental spikes in a given dataset ("false" peaks). LHO calibration was found to be off by $\approx 90^o$, therefore, a new method to select a single-trip region was invented. Next steps of this project could examine the possibilities to extend the range of a good algorithm performance, and could investigate the limiting factors to achieve it, whether they come from the paraxial approximation not being held or maybe due to the computational issues. Also, an information from the optical-lever sensor could be used to improve the accuracy in the small-misalignment region.

Acknowledgements

I would like to thank Michael Landry and Keita Kawabe for selecting me for this project. Keita was guiding me throughout the summer, giving me a lot of lectures about interferometry, and also sharing his ideas for every step of the code, for which I am very grateful. Both Michael and Keita were helping me a lot to prepare the reports and presentations. I would also like to thank Caltech Student-Faculty Programs (SFP) and National Science Foundation (NSF) for organising and funding this internship and for providing such a great opportunity to gain experience in physics research.

A Mode Decomposition Coefficients

Table 3: Higher-order Hermite-Gaussian mode power coefficients for $m + n \leq 10$.

$\lvert i\frac{\alpha}{\alpha_0} + \frac{a}{w_0}\rvert$	Mode 0	Mode 1	Mode 2	Mode 3	Mode 4	Mode 5	Mode 6	Mode 7	Mode 8	Mode 9	Mode 10
0	1	0	1.7948e-17	0	3.2212e-34	0	5.7814e-51	0	1.0376e-67	0	1.8623e-84
0.020013	0.9996	0.00040012	8.008e-08	1.0685e-11	1.0692e-15	8.5598e-20	5.7105e-24	3.2654e-28	1.6338e-32	7.2666e-37	2.9087e-41
0.040026	0.9984	0.0015986	1.2797e-06	6.83e-10	2.7339e-13	8.7547e-17	2.3362e-20	5.3436e-24	1.0695e-27	1.9026e-31	3.0463e-35
0.060039	0.9964	0.0035896	6.4657e-06	7.7643e-09	6.9927e-12	5.0383e-15	3.0251e-18	1.5568e-21	7.0107e-25	2.8062e-28	1.011e-31
0.080053	0.99362	0.0063636	2.0378e-05	4.3503e-08	6.9653e-11	8.9218e-14	9.5233e-17	8.7131e-20	6.9753e-23	4.9637e-26	3.179e-29
0.10007	0.99004	0.0099073	4.9571e-05	1.6535e-07	4.1367e-10	8.2792e-13	1.3808e-15	1.974e-18	2.4692e-21	2.7455e-24	2.7474e-27
0.12008	0.98569	0.014204	0.00010234	4.9157e-07	1.7709e-09	5.1038e-12	1.2258e-14	2.5233e-17	4.5451e-20	7.2773e-23	1.0487e-25
0.14009	0.98058	0.019233	0.00018861	1.2331e-06	6.0466e-09	2.3719e-11	7.7536e-14	2.1725e-16	5.3264e-19	1.1608e-21	2.2767e-24
0.16011	0.97471	0.02497	0.00031984	2.7312e-06	1.7492e-08	8.9621e-11	3.8265e-13	1.4004e-15	4.4844e-18	1.2764e-20	3.27e-23
0.18012	0.9681	0.031388	0.00050885	5.4994e-06	4.4576e-08	2.8905e-10	1.562e-12	7.2348e-15	2.9321e-17	1.0563e-19	3.4248e-22
0.20013	0.96076	0.038457	0.00076968	1.027e-05	1.0277e-07	8.2272e-10	5.4886e-12	3.1385e-14	1.5704e-16	6.9843e-19	2.7957e-21
0.22014	0.95272	0.046144	0.0011175	1.8041e-05	2.1845e-07	2.1161e-09	1.7081e-11	1.1819e-13	7.1554e-16	3.8507e-18	1.865e-20
0.24016	0.94399	0.054412	0.0015682	3.013e-05	4.3417e-07	5.0051e-09	4.8083e-11	3.9593e-13	2.8527e-15	1.827e-17	1.0531e-19
0.26017	0.93459	0.063222	0.0021384	4.8219e-05	8.1547e-07	1.1033e-08	1.2439e-10	1.2021e-12	1.0165e-14	7.6403e-17	5.1684e-19
0.28018	0.92454	0.072535	0.0028454	7.4411e-05	1.4595e-06	2.29e-08	2.9944e-10	3.3561e-12	3.2913e-14	2.8691e-16	2.2509e-18
0.3002	0.91387	0.082306	0.0037064	0.00011127	2.5053e-06	4.5127e-08	6.7737e-10	8.7152e-12	9.8114e-14	9.8183e-16	8.8426e-18
0.32021	0.9026	0.092491	0.0047389	0.00016187	4.1467e-06	8.4983e-08	1.4514e-09	2.1247e-11	2.7215e-13	3.0986e-15	3.1752e-17
0.34022	0.89076	0.10304	0.0059601	0.00022982	6.6465e-06	1.5377e-07	2.9648e-09	4.8996e-11	7.0848e-13	9.1064e-15	1.0534e-16
0.36024	0.87837	0.11392	0.0073869	0.00031934	1.0354e-05	2.6856e-07	5.8049e-09	1.0755e-10	1.7435e-12	2.5124e-14	3.2583e-16
0.38025	0.86545	0.12506	0.0090356	0.00043522	1.5722e-05	4.5438e-07	1.0943e-08	2.259e-10	4.0803e-12	6.5511e-14	9.4664e-16
0.40026	0.85205	0.13642	0.010921	0.00058289	2.3332e-05	7.4714e-07	1.9938e-08	4.5603e-10	9.127e-12	1.6237e-13	2.5998e-15
0.42028	0.83818	0.14796	0.013059	0.00076841	3.391e-05	1.1972e-06	3.5222e-08	8.8822e-10	1.9599e-11	3.8441e-13	6.7857e-15
0.44029	0.82388	0.15961	0.015461	0.00099847	4.836e-05	1.8738e-06	6.0504e-08	1.6745e-09	4.0552e-11	8.7292e-13	1.6912e-14
0.4603	0.80917	0.17134	0.01814	0.0012804	6.778e-05	2.8705e-06	1.013e-07	3.0644e-09	8.1109e-11	1.9083e-12	4.0408e-14
0.48032	0.79409	0.18309	0.021106	0.0016221	9.3498e-05	4.3114e-06	1.6567e-07	5.4568e-09	1.5727e-10	4.0288e-12	9.2889e-14
0.50033	0.77866	0.1948	0.024367	0.002032	0.00012709	6.359e-06	2.6514e-07	9.476e-09	2.9633e-10	8.2372e-12	2.0607e-13
0.52034	0.76293	0.20644	0.02793	0.0025192	0.00017042	9.2226e-06	4.1592e-07	1.6078e-08	5.4381e-10	1.635e-11	4.4241e-13
0.54035	0.74692	0.21795	0.0318	0.0030931	0.00022564	1.3169e-05	6.4045e-07	2.6698e-08	9.7382e-10	3.1574e-11	9.2133e-13
0.56037	0.73065	0.22929	0.035978	0.0037635	0.00029527	1.8532e-05	9.6929e-07	4.3455e-08	1.7046e-09	5.9438e-11	1.8653e-12
0.58038	0.71417	0.24041	0.040466	0.0045408	0.00038214	2.5729e-05	1.4435e-06	6.942e-08	2.9212e-09	1.0926e-10	3.6782e-12
0.60039	0.6975	0.25128	0.045261	0.0054351	0.0004895	3.5269e-05	2.1176e-06	1.0898e-07	4.9076e-09	1.9644e-10	7.0768e-12
0.62041	0.68068	0.26183	0.05036	0.0064573	0.00062098	4.7774e-05	3.0629e-06	1.6831e-07	8.0931e-09	3.4591e-10	1.3306e-11
0.64042	0.66373	0.27205	0.055755	0.0076178	0.0007806	6.3992e-05	4.3716e-06	2.5598e-07	1.3115e-08	5.973e-10	2.4483e-11
0.66043	0.64668	0.28189	0.061439	0.0089271	0.00097284	8.4813e-05	6.1617e-06	3.837e-07	2.0907e-08	1.0126e-09	4.4141e-11
0.68045	0.62957	0.29132	0.067399	0.010396	0.0012026	0.00011129	8.5829e-06	5.6736e-07	3.2816e-08	1.6872e-09	7.8071e-11
0.70046	0.61242	0.30029	0.073623	0.012034	0.0014751	0.00014466	1.1823e-05	8.2816e-07	5.076e-08	2.7655e-09	1.3561e-10
0.72047	0.59526	0.3088	0.080096	0.01385	0.0017962	0.00018637	1.6113e-05	1.1941e-06	7.7434e-08	4.4633e-09	2.3154e-10
0.74049	0.57811	0.3168	0.0868	0.015855	0.0021721	0.00023805	2.1741e-05	1.702e-06	1.1658e-07	7.0983e-09	3.8897e-10
0.7605	0.56102	0.32427	0.093715	0.018056	0.0026091	0.00030161	2.9055e-05	2.3992e-06	1.7334e-07	1.1132e-08	6.4345e-10
0.78051	0.54399	0.33119	0.10082	0.020461	0.0031142	0.0003792	3.8478e-05	3.3466e-06	2.5469e-07	1.7229e-08	1.0489e-09
0.80053	0.52706	0.33755	0.10809	0.023076	0.0036947	0.00047325	5.0515e-05	4.6218e-06	3.7e-07	2.633e-08	1.6863e-09
0.82054	0.51024	0.34333	0.11551	0.025907	0.004358	0.00058648	6.577e-05	6.3221e-06	5.3175e-07	3.9755e-08	2.675e-09
0.84055	0.49357	0.34851	0.12304	0.028959	0.0051119	0.0007219	8.4955e-05	8.5694e-06	7.5635e-07	5.9339e-08	4.1899e-09
0.86056	0.47706	0.35308	0.13066	0.032234	0.0059643	0.00088286	0.0001089	1.1514e-05	1.0653e-06	8.7601e-08	6.4835e-09
0.88058	0.46073	0.35704	0.13834	0.035736	0.0069233	0.001073	0.00013859	1.5343e-05	1.4862e-06	1.2797e-07	9.9168e-09
0.90059	0.44461	0.36038	0.14606	0.039463	0.0079968	0.0012964	0.00017514	2.028e-05	2.0548e-06	1.8506e-07	1.5e-08
0.9206	0.4287	0.36311	0.15377	0.043415	0.0091931	0.0015573	0.00021984	2.66e-05	2.8162e-06	2.6504e-07	2.2448e-08
0.94062	0.41304	0.36521	0.16146	0.04759	0.01052	0.0018604	0.00027416	3.4632e-05	3.8277e-06	3.7606e-07	3.3252e-08
0.96063	0.39763	0.36671	0.1691	0.051983	0.011985	0.0022107	0.00033979	4.4768e-05	5.1608e-06	5.2884e-07	4.8772e-08
0.98064	0.38248	0.36759	0.17664	0.056588	0.013596	0.0026134	0.00041861	5.7474e-05	6.9045e-06	7.3731e-07	7.086e-08
1.0007	0.36762	0.36788	0.18407	0.061399	0.01536	0.0030742	0.00051273	7.3298e-05	9.1687e-06	1.0195e-06	1.0202e-07

B Code

Full collection of scripts written in the project can be downloaded from `https://github.com/lsinkunaite/Cavity_Alignment/blob/master/Project.zip`.

References

[1] *Gaussian beam*, https://upload.wikimedia.org/wikipedia/commons/thumb/5/53/GaussianBeamWaist.svg/416px-GaussianBeamWaist.svg.png.

[2] Y. Hefetz, N. Mavalvala, and D. Sigg, *Principles of calculating alignment signals in complex resonant optical interferometers*, J. Opt. Soc. Am. B **14 (7)**, 1597-1605 (Jul 1997).

[3] D. Anderson, *Alignment of resonant optical cavities*, Appl. Opt. **23 (17)**, 2944-2949 (1984).

[4] *MATLAB*, http://www.mathworks.com/?refresh=true.

[5] *Finesse manual*, http://www.gwoptics.org/finesse/.

[6] *E2E software*, http://www.ligo.caltech.edu/~e2e/.

[7] H. Kogelnik and T. Li, *Laser beams and resonators*, Appl. Opt. **5 (10)**, 1550-1567 (1966).

[8] P.Fulda, *Precision Interferometry in a New Shape: Higher-order Laguerre-Gauss Modes for Gravitational Wave Detection*, Springer (2014).

[9] *Numerical modelling tools for GW detectors*, https://gwic.ligo.org/simulations/.